Carbon dioxide and oxygen fluxes in the Southern Ocean: Mechanisms of interannual variability

A. Verdy,[1] S. Dutkiewicz,[2] M. J. Follows,[2] J. Marshall,[2] and A. Czaja[3]

Received 20 December 2006; accepted 15 February 2007; published 31 May 2007.

[1] We analyze the variability of air-sea fluxes of carbon dioxide and oxygen in the Southern Ocean during the period 1993–2003 in a biogeochemical and physical simulation of the global ocean. Our results suggest that the nonseasonal variability is primarily driven by changes in entrainment of carbon-rich, oxygen-poor waters into the mixed layer during winter convection episodes. The Southern Annular Mode (SAM), known to impact the variability of air-sea fluxes of carbon dioxide, is also found to affect oxygen fluxes. We find that El Niño–Southern Oscillation (ENSO) also plays an important role in generating interannual variability in air-sea fluxes of carbon and oxygen. Anomalies driven by SAM and ENSO constitute a significant fraction of the simulated variability; the two climate indices are associated with surface heat fluxes, which control the modeled mixed layer depth variability. We adopt a Lagrangian view of tracers advected along the Antarctic Circumpolar Current (ACC) to highlight the importance of convective mixing in inducing anomalous air-sea fluxes of carbon dioxide and oxygen. The idealized Lagrangian model captures the principal features of the variability simulated by the more complex model, suggesting that knowledge of entrainment, temperature, and mean geostrophic flow in the mixed layer is sufficient to obtain a first-order description of the large-scale variability in air-sea transfer of soluble gases. Distinct spatial and temporal patterns arise from the different equilibration timescales of the two gases.

Citation: Verdy, A., S. Dutkiewicz, M. J. Follows, J. Marshall, and A. Czaja (2007), Carbon dioxide and oxygen fluxes in the Southern Ocean: Mechanisms of interannual variability, *Global Biogeochem. Cycles*, *21*, GB2020, doi:10.1029/2006GB002916.

1. Introduction

[2] Deep waters in the Southern Ocean are rich in dissolved inorganic carbon (DIC) and depleted in oxygen. When circulation brings these waters into the mixed layer, the soluble gases are exchanged at the air-sea interface. The formation of deep mixed layers combined with high biological productivity makes the Southern Hemisphere extratropical oceans an important component of the global carbon cycle.

[3] Variability of the circulation and biology of the Southern Ocean has been suggested to impact local air-sea exchange of carbon dioxide. *Le Quéré et al.* [2003] described how ocean pCO_2 responds to changes in stratification through variations in supply of DIC and in the average light available to phytoplankton. *Lovenduski and Gruber* [2005] examined how the Southern Annular Mode (SAM), a dominant mode of local atmospheric variability, is related to observed variability in primary production; they speculate that the biological response to SAM would largely compensate the supply of DIC resulting from SAM-induced changes in ocean circulation. More recent modeling studies, however, suggest that SAM drives about a third of regional CO_2 air-sea flux variability on an interannual timescale, primarily because of changes in the physical circulation [*Lenton and Matear*, 2007; *Lovenduski et al.*, 2007]. In the region of the Antarctic Circumpolar Current (ACC) the oceanic response to SAM during its positive phase consists of northward Ekman currents, upwelling near the coast of Antarctica, and intensification of the geostrophic zonal flow [*Hall and Visbeck*, 2002].

[4] While these studies focused on SAM, there is also evidence for El Niño–Southern Oscillation (ENSO)-related physical variability in the Southern Ocean. Both SAM and ENSO are important sources of sea surface temperature (SST) variability in the ACC [*Verdy et al.*, 2006]. Sea ice variability in the Southern Ocean is thought to be strongly influenced by ENSO teleconnections [*Yuan*, 2004, and references therein]. ENSO is also the main driver of CO_2 air-sea flux variability in the equatorial Pacific, where it modulates convective mixing and biological export production [*Feely et al.*, 2002; *McKinley et al.*, 2004].

[5] In this study we investigate the interannual variability of air-sea fluxes of CO_2 and O_2 in the Southern Ocean,

[1]MIT–WHOI Joint Program in Oceanography, Massachusetts Institute of Technology, Cambridge, Massachusetts, USA.
[2]Department of Earth, Atmospheric and Planetary Sciences, Massachusetts Institute of Technology, Cambridge, Massachusetts, USA.
[3]Space and Atmospheric Physics Group, Department of Physics, Imperial College London, London, UK.

0886-6236/07/2006GB002916$12.00

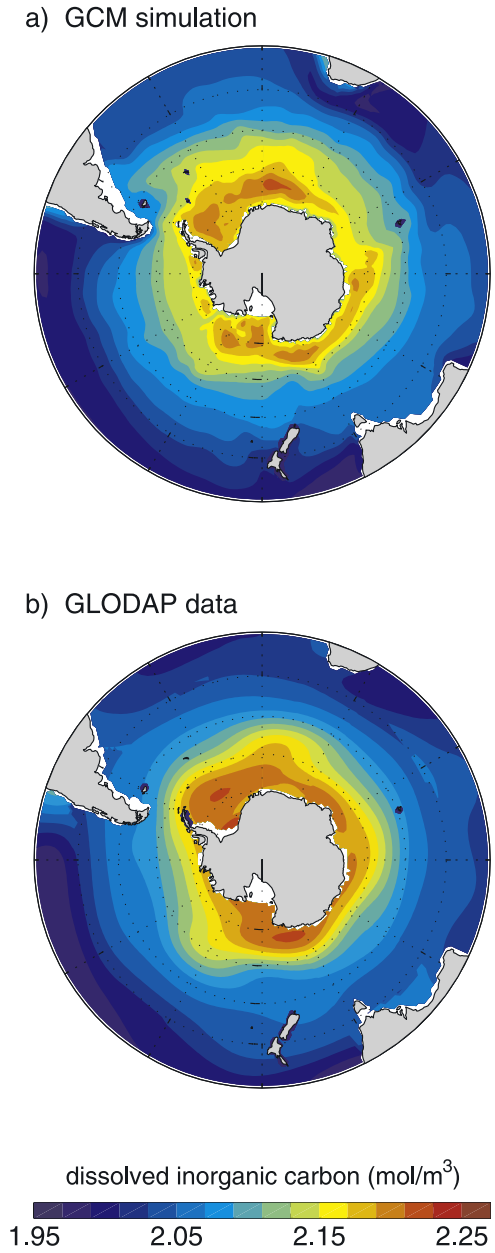

Figure 1. Dissolved inorganic carbon concentration at 100 m from (a) the global circulation model (GCM) simulation and (b) Global Ocean Data Analysis Project (GLODAP), calculated as total CO_2 minus anthropogenic CO_2.

addressing the respective roles of ENSO and SAM. Variations in these climatic indices reflect large-scale patterns in anomalous surface heat fluxes, convective mixing, and entrainment of DIC and oxygen into the mixed layer. Comparing the response of the two gases, which have different air-sea equilibration timescales, affords a more complete picture of the ocean-atmosphere interactions regulating the variability of air-sea fluxes in a global physical-biogeochemical model.

[6] We then apply a Lagrangian theoretical framework to investigate the mechanisms responsible for air-sea fluxes of CO_2 and O_2. Using a highly simplified model of tracers propagating in the ocean mixed layer, we are able to idealize the physical and biogeochemical systems and focus on the key mechanisms. The idealized Lagrangian model captures the behavior of the complex three-dimensional system and clearly illustrates how changes in entrainment due to mixed layer depth variations are the primary driver of the large-scale variability in gas fluxes in the region of the ACC.

2. Air-Sea Fluxes of Carbon and Oxygen in a Global Ocean Model

2.1. Model Description

[7] Air-sea fluxes of CO_2 and O_2 are simulated in a global numerical ocean model (hereinafter referred to as global circulation model (GCM)) for the period 1993–2003. Temperature, salinity, and flow fields are obtained from the Estimating the Circulation and Climate of the Ocean (ECCO) state estimation project [*Wunsch and Heimbach*, 2006], which uses available observations to constrain the MIT general circulation model [*Marshall et al.*, 1997]. An iterative data assimilation procedure serves to determine the initial conditions, surface fluxes, and model parameters that minimize the misfit between data and model; the data sets used are listed in the appendix of *Wunsch and Heimbach* [2006] and include measurements of sea surface temperature and salinity, altimetry data, and float profiles.

[8] The model has a horizontal resolution of 1°; there are 23 vertical levels whose thickness ranges from 10 m near the surface to 500 m at depth, with 13 levels in the top kilometer of the water column. We use the GM/Redi parameterization of geostrophic eddy fluxes [*Gent and McWilliams*, 1990; *Redi*, 1982] and the K profile parameterization (KPP) vertical mixing scheme [*Large et al.*, 1994] to account for subgrid-scale processes. The flow fields transport biogeochemical tracers of inorganic and organic forms of carbon, phosphorus, iron, and oxygen as well as alkalinity. We do not resolve the ocean ecosystem; instead, the biogeochemical model adopts a simple carbon export scheme with limitation by phosphate, iron, and light availability. The net community production of organic matter is given by

$$\beta \frac{\mathrm{I}}{\mathrm{I}+\kappa_{\mathrm{I}}} \min\left(\frac{\mathrm{PO_4}}{\mathrm{PO_4}+\kappa_{\mathrm{PO4}}}, \frac{\mathrm{Fe}}{\mathrm{Fe}+\kappa_{\mathrm{Fe}}}\right), \tag{1}$$

where β is maximum community production and κ_{I}, κ_{PO4}, and κ_{Fe} are half-saturation coefficients. Two thirds of net production is assumed to enter the dissolved organic pool, the remaining fraction of organic production being exported to depth as sinking particles. Surface carbonate chemistry is explicitly solved [*Follows et al.*, 2006], and air-sea transfer of CO_2 and O_2 is parameterized following *Wanninkhof* [1992]. Aspects of this model are described in more detail by *McKinley et al.* [2003], *Dutkiewicz et al.* [2005], and *Parekh et al.* [2006]. Modeled phosphate, oxygen, iron, DIC, and alkalinity distributions capture the observed large-scale horizontal and vertical gradients; in Figure 1 the annual mean DIC concentration at 100 m in the GCM is shown next to observations from the Global Ocean Data Analysis Project [*Key et al.*, 2004].

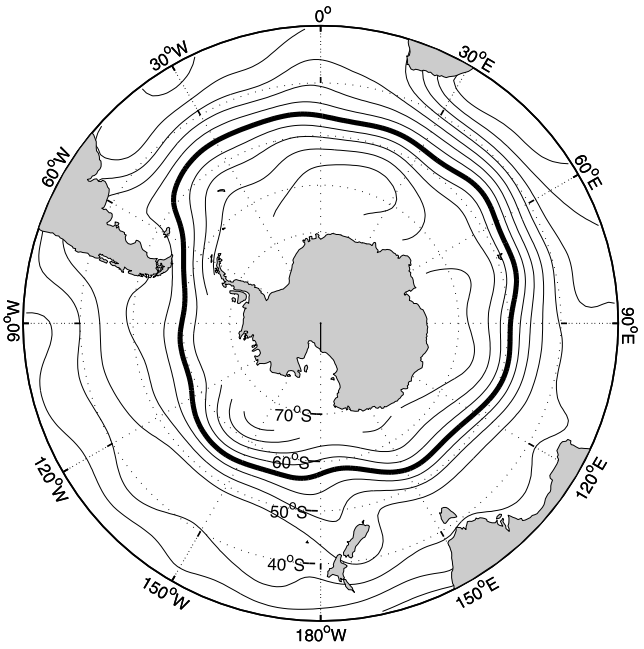

Figure 2. Geostrophic streamlines in the Southern Ocean. Contour interval is 2×10^3 m^2/s. Thick curve indicates streamline along which the simulated variability is plotted in Figures 3 and 4.

[9] Results used in this 11 year study were obtained after 120 years of spin-up of the biogeochemistry model with preindustrial atmospheric CO_2. The analysis is performed on monthly averaged fields, from which the long-term trend and mean seasonal cycle are removed. We focus on the region of the ACC, where the nonseasonal variability of air-sea fluxes is largest in our model. In order to examine the advection of anomalies by the mean flow we analyze the variability along geostrophic streamlines, estimated from the mean sea surface height (Figure 2). This procedure will facilitate the comparison of GCM results with results from the one-dimensional Lagrangian model (section 4). Here we will show the variability along the circumpolar streamline indicated by the thick curve in Figure 2, with a mean latitude of 52°S.

2.2. Simulated Variability

[10] The variability of CO_2 and O_2 fluxes is presented in Figure 3. The time-longitude diagrams highlight three features of the simulated variability: First, there is eastward propagation of the anomalies; second, oxygen fluxes have a larger amplitude and are more localized in time and space than carbon fluxes; third, O_2 and CO_2 fluxes tend to have opposite signs.

[11] This anticorrelation in the large-scale patterns of carbon and oxygen fluxes suggests that the variability is primarily driven by entrainment [*Gruber et al.*, 2002]. Comparison with surface heat flux (not shown) reveals that heating of the ocean occurs simultaneously with outgassing of O_2 and intake of CO_2. If thermal solubility was the dominant cause of air-sea fluxes, warming would result in outgassing of both gases. The two fields exhibit more variance in the Pacific during the austral winter and spring; this timing and location correspond to that of mode water formation, associated with the deepest mixed layers, reinforcing the idea that entrainment is the dominant term driving anomalous fluxes.

[12] Dissolved oxygen adjusts rapidly to the atmospheric concentration, the equilibration timescale being roughly 1 month. This causes large air-sea fluxes and results in rapid dissipation of the anomalies generated in wintertime, so the variability of O_2 appears localized in time and space. In contrast, carbonate chemistry causes the equilibration timescale for carbon to be much longer, on the order of 1 year (depending on the depth of the mixed layer); the amplitude of anomalous carbon fluxes is thus weaker and relatively constant throughout the year. The slowly decaying anomalies are then able to propagate with the mean flow. Estimation from Figure 3b suggests that model anomalies travel eastward at a speed of roughly 8 cm/s, which corresponds to the observed propagation speed of SST anomalies and coincides with the mean geostrophic flow in the ACC [*Verdy et al.*, 2006].

[13] In Figure 4 the variability of simulated mixed layer depth (MLD) and SST is shown along the same geostrophic streamline. We identify the MLD from the density profile as the depth at which potential density exceeds the surface value by at least 0.15 kg/m^3. The similitude between anomalous MLD and anomalous O_2 fluxes (Figure 3a) is most apparent during winter months, when convection events cause the mixed layers to deepen. Interannual variability in MLD impacts the strength of convective mixing, and deeper mixed layers are associated with enhanced entrainment of oxygen-depleted water into the mixed layer. Anomalous CO_2 fluxes (Figure 3b) are also consistent with changes in MLD, but because of the longer equilibration time they appear to be more similar to SST variability (Figure 4b); SST anomalies have a decay timescale of approximately 8 months for a 100 m thick mixed layer. Unlike CO_2, SST exhibits more variability during the austral summer, when the mixed layer is shallow; this suggests that thermal effects are dominant over entrainment in inducing temperature changes, which is consistent with the results of *Verdy et al.* [2006].

[14] The propagation speed of SST anomalies matches that of CO_2 anomalies. Despite a decay timescale of a few months, anomalies are occasionally found to persist for several years; the interplay between mean oceanic advection and random heat flux forcing is thought to explain the long persistence [*Verdy et al.*, 2006, and references therein]. We also find a hint of propagation of MLD anomalies in the GCM (Figure 4a) that is likely to result from the same mechanism since temperature and stratification are both affected by heat flux variability. In turn, propagation of the MLD signal explains the persistence of CO_2 and O_2 anomalies, which during some periods, are found to last for up to 5 years (Figure 3). Successive years of anomalously large or weak entrainment seem to reinforce air-sea flux anomalies generated in the previous winter.

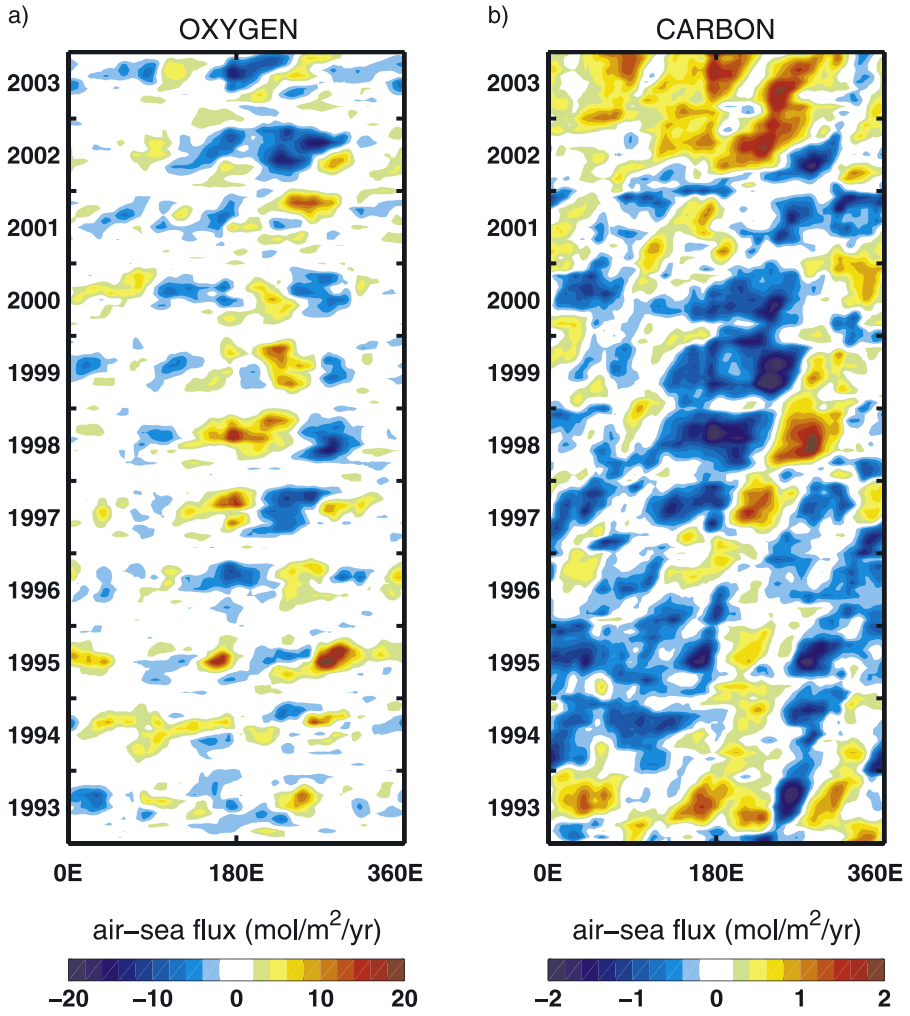

Figure 3. Air-sea flux variability of (a) oxygen and (b) carbon dioxide from the GCM simulation. The time-longitude diagrams show deviations from the mean seasonal cycle, for the period 1993–2003, along a geostrophic streamline. Positive values indicate fluxes into the ocean.

[15] The large-scale patterns of variability along other streamlines in the region of the ACC, extending roughly from 55° to 65°S, are very similar to the ones presented here. Farther south, the simulated variability is more complex, and since nearshore processes are not well resolved in the model, it is not discussed here; farther north, air-sea flux anomalies are weak and do not propagate eastward.

3. Modes of Air-Sea Flux Variability, ENSO and SAM

[16] The spatial patterns of variability are identified by the first three empirical orthogonal functions (EOF) of air-sea flux of CO_2 and O_2 south of 30°S. To focus on interannual variability, time series are filtered with a 12 month running mean. We then examine the influence of two modes of climate variability, ENSO and SAM. The spatial patterns are presented in Figure 5; the associated time series, shown in Figure 6, are compared to indices of ENSO and SAM variability. The Niño3 index is calculated from the SST averaged between 5°S and 5°N, from 150° to 90°W [*Cane et al.*, 1986]. For the SAM index we use the time series of the NOAA Climate Prediction Center, constructed by projecting the 700 hPa height anomalies poleward of 20°S onto the leading EOF mode of mean 700 hPa height, consistent with *Thompson and Wallace* [2000].

[17] The first three EOFs of oxygen fluxes are associated with 29, 16, and 14% of the variance, respectively. The first mode (Figure 5a) appears as a wide zone of ingassing over most of the South Pacific basin and a narrow band of outgassing centered on Drake Passage. It is associated with SAM, the time series having a correlation coefficient of r = 0.75 (no lag). The second EOF (Figure 5b) reflects the influence of ENSO. It shows outgassing in the eastern Pacific; the maximum correlation occurs for a 3 month lag, the correlation coefficient being r = 0.75. These values are significant at the 99% level. The third EOF is not significantly correlated to either SAM or ENSO. In Figures 6a and 6b the time series corresponding to the first

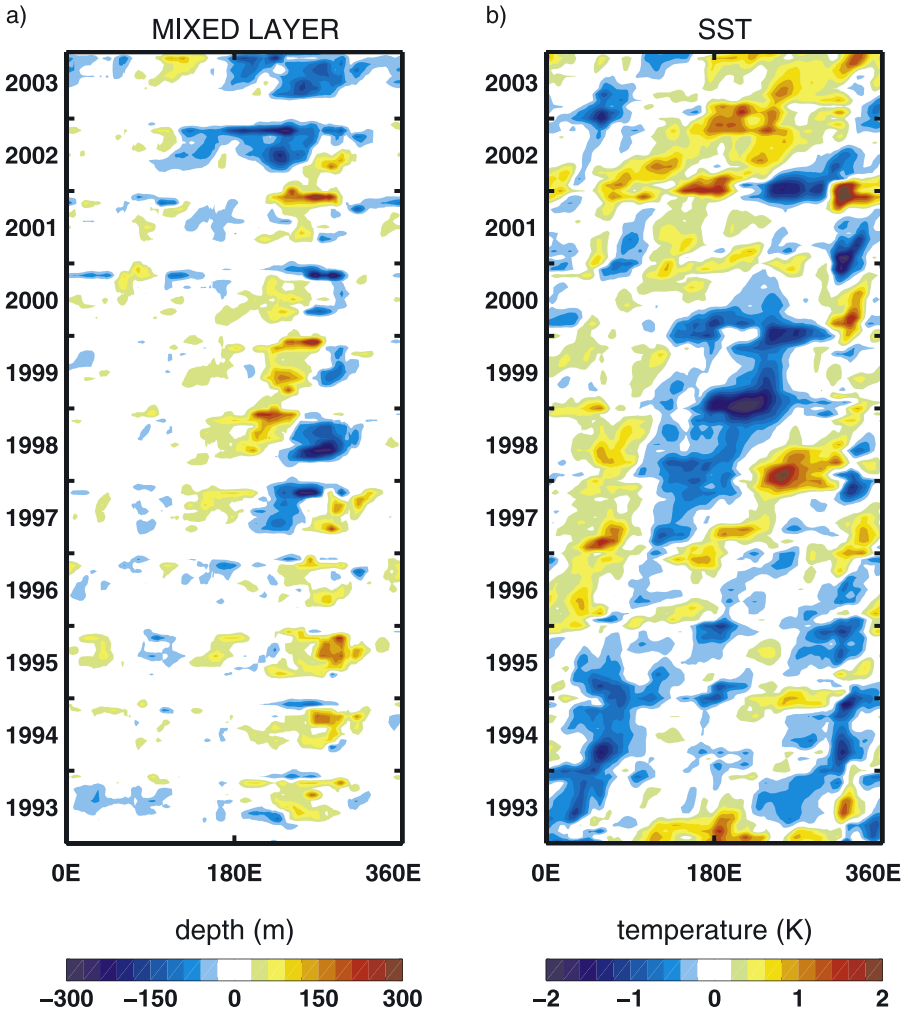

Figure 4. Time-longitude diagrams of anomalous (a) mixed layer depth and (b) sea surface temperature (SST), along a geostrophic streamline. Positive values indicate deep mixed layers and high temperatures.

and second EOFs are overlain on the SAM index and Niño3 index, also smoothed with a 12 month running mean.

[18] The first three EOFs of carbon dioxide fluxes are associated with 31, 22, and 17% of the variance, respectively. The spatial patterns for the first and third modes of variability shown in Figures 5c and 5d are similar to the patterns of O_2 variability described above. The second EOF, not shown, is not significantly correlated to SAM or ENSO. The first mode is once again linked to SAM; with a 3 month lag, the correlation coefficient $r = 0.71$ is significant at the 95% level. The third mode appears to indicate ENSO-related variability, the maximum correlation occurring for a 6 month lag; the correlation coefficient with Niñõ3 is $r = 0.80$, which is significant at the 99% level. The time series are shown in Figures 6c and 6d together with indices for SAM and ENSO.

[19] Although the fraction of variance explained by the ENSO-related EOF is less than that explained by the SAM-related EOF, the magnitude of the induced fluxes is comparable. Both flux patterns have a dipole structure in the Pacific basin, a feature that is also seen in Figure 3. This reflects the spatial patterns of atmospheric forcing induced by SAM and ENSO: both are associated with anomalous winds over the Southern Ocean that cause surface fluxes of sensible and latent heat. During the positive phase of the SAM and during El Ninõ events, surface pressure over the South Pacific is anomalously low; the resulting zonal pressure gradients drive meridional winds and thus heat fluxes which, in turn, induce changes in solubility and convective mixing. The ENSO and SAM heat flux patterns are shown by *Verdy et al.* [2006] and are discussed in relation to their role in generating SST anomalies. In the case of SST both surface heat fluxes and oceanic Ekman advection of heat contribute to the observed variability; in contrast, the role of Ekman advection in driving gas flux variability is found to be small compared to that of surface heat fluxes (an explanation is given in section 4.2).

4. Mechanisms

4.1. Diagnostic Framework

[20] DIC and oxygen are biologically active tracers affected by air-sea fluxes, entrainment, biological production, advection, and dilution by evaporation and precipitation. Averaged over the depth of the mixed layer, the time

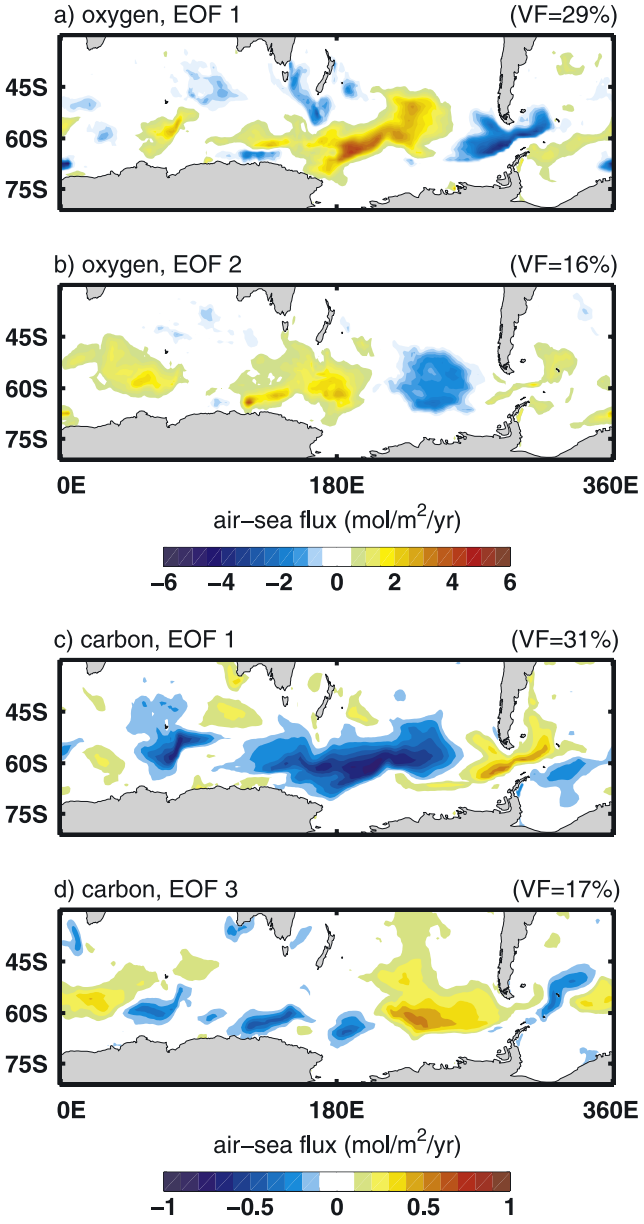

Figure 5. Spatial patterns of the leading empirical orthogonal functions (EOF) for air-sea flux variability of (a, b) oxygen and (c, d) carbon dioxide and fraction of the total variance (VF) associated with each mode. Southern Annular Mode (SAM) is associated with the first EOF of O_2 and CO_2 fluxes; El Niño–Southern Oscillation (ENSO) is associated with the second empirical orthogonal function (EOF) of O_2 fluxes and the third EOF of CO_2 fluxes. The second EOF of CO_2 fluxes, not shown, is not correlated with SAM or ENSO.

development of the tracer concentration C can be described by the following simple differential equation [see *Williams and Follows*, 1998]:

$$\frac{DC}{Dt} = \frac{F}{h} + \Lambda(C_{th} - C)\frac{1}{h}\frac{\partial h}{\partial t} + \frac{1}{h}(E - P)C + B, \qquad (2)$$

where h is the mixed layer depth, F is the air-sea flux, E and P are the evaporation and precipitation, respectively, B is the biological production, and $D/Dt \equiv \partial/\partial t + \mathbf{u} \cdot \nabla$ is the Lagrangian derivative. Here the value of B is tracer-dependent, as biological production produces O_2 but uses DIC.

[21] Equation (2) is an idealized description of the processes that change the concentration of dissolved gas, following a parcel of fluid. Each term on the right-hand side expresses a mechanism through which an amount of tracer is added to or removed from the surface waters. The first term represents fluxes to the atmosphere. The second term represents the entrainment from the thermocline when the mixed layer is deepening; C_{th} is the concentration in the thermocline, and Λ is a heaviside function; we set $\Lambda = 1$ when $\partial h/\partial t > 0$, i.e., when the mixed layer is deepening, and 0 otherwise because shoaling of the mixed layer does not affect C. The rate of change of h can be related to the surface heat fluxes and wind stress [*Kraus and Turner*, 1967]. The third term accounts for dilution of the tracer concentration by addition of freshwater; the fourth term represents uptake or release of tracer resulting from biological activities.

[22] When the tracer in the mixed layer is at equilibrium with the atmosphere, its concentration is equal to the saturation concentration C^{sat}. Departures from this equilibrium are defined as

$$\Delta C = C - C^{sat} \qquad (3)$$

and drive the air-sea flux, which can be written as

$$F = -K\Delta C, \qquad (4)$$

where K is the gas transfer coefficient. F is defined as positive when the flux is into the ocean.

[23] Assuming that the saturation concentration is a function of temperature only allows some simplifications to be made. This is a reasonable assumption in the case of oxygen, and although alkalinity strongly affects the solubility of DIC, in the ACC region its effect appears to be small compared to the effect of temperature [*Lovenduski et al.*, 2007]. For the two tracers in Southern Ocean conditions the dependence of solubility on temperature is close to linear. As done by *Takahashi et al.* [1993] we write

$$\frac{DC^{sat}}{Dt} = \frac{\partial C^{sat}}{\partial T}\frac{DT}{Dt} \approx \alpha\frac{DT}{Dt} \qquad (5)$$

$$\frac{DT}{Dt} = \frac{H}{\rho c_p h} + \Lambda(T_{th} - T)\frac{1}{h}\frac{\partial h}{\partial t}, \qquad (6)$$

where T is the sea surface temperature, T_{th} the temperature in the thermocline, α is a negative constant (resulting from a linear approximation of the reduction of solubility with increasing temperature) that is tracer-dependent, H is the sum of sensible and latent surface heat fluxes, and ρ and c_p are the density and heat capacity of seawater, respectively.

[24] Because we are interested in diagnosing the air-sea gas fluxes, it is convenient to derive an equation for ΔC,

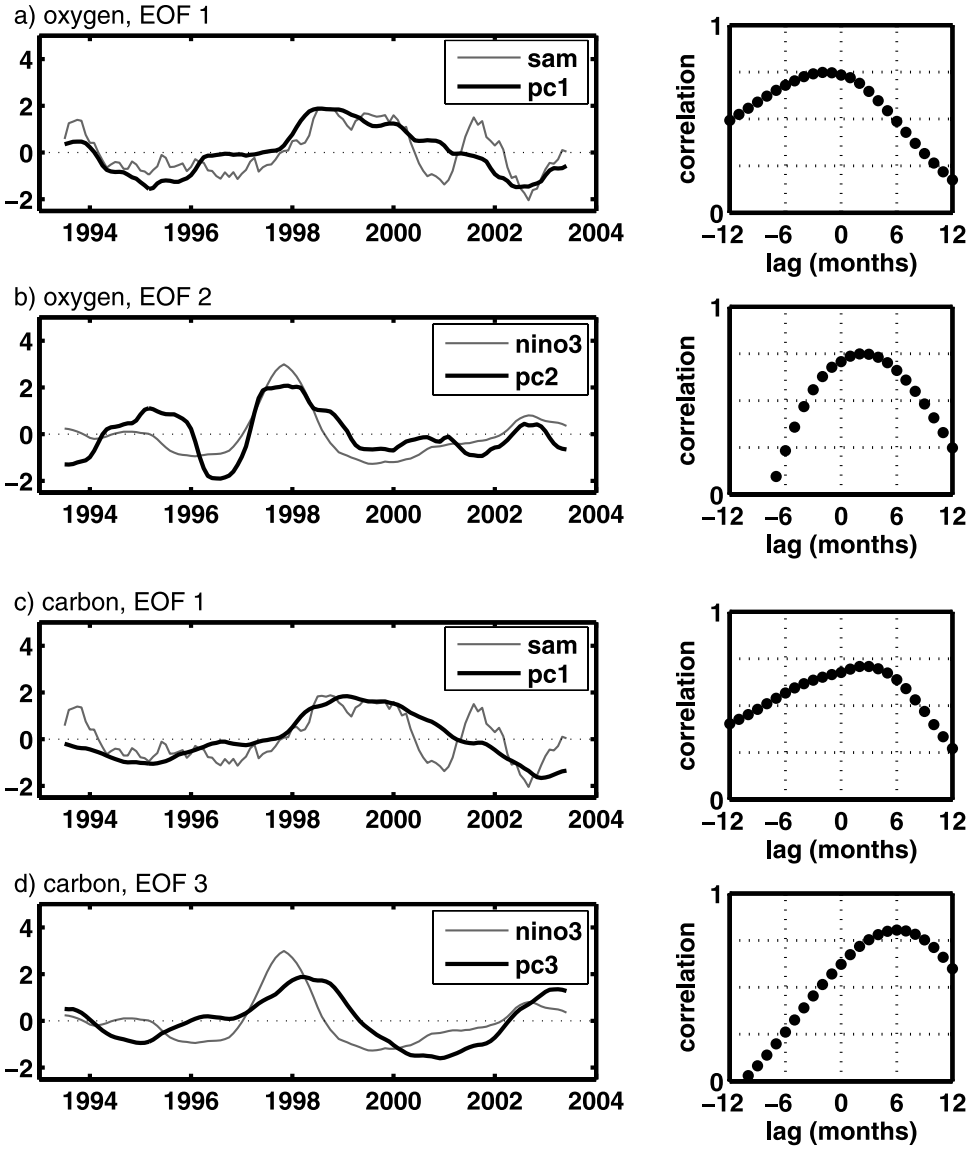

Figure 6. Principal components associated with the EOFs of Figure 4 along with (a, c) the SAM index and (b, d) the Niño3 index. All time series are filtered with a 12 month running mean and normalized. Figures 6a–6d show the lagged correlations (right) between the time series (left); for positive lags the climate index leads.

which is directly related to the flux according to (4). We substitute (3) into (2) and, making use of (5) and (6), obtain a prognostic equation for the disequilibrium concentration:

$$\frac{D\Delta C}{Dt} = \frac{F}{h} - \Lambda\left(C^{\dagger} - \alpha T^{\dagger}\right)\frac{1}{h}\frac{\partial h}{\partial t} - \alpha\frac{H}{\rho c_p h} + \frac{1}{h}(E-P)C + B, \tag{7}$$

where we have defined $X^{\dagger} = X - X_{th}$, the anomaly relative to the thermocline value. In addition to the four mechanisms involved in changes to the tracer concentration that appeared in (2), changes in solubility resulting from heat fluxes and entrainment also affect the disequilibrium concentration.

4.2. Lagrangian Model

[25] We now address the relative importance of thermodynamics, entrainment, advection, dilution, and biological production in generating the air-sea flux variability described in section 2. We substitute (4) into (7) to obtain an equation for the air-sea flux from which we remove the mean seasonal cycle. With a view to reducing the complexity of the model as much as possible we assume a constant value for K. This yields

$$\frac{\partial F'}{\partial t} + \overline{\mathbf{u}}\cdot\nabla F' = -\frac{K}{h}F' + K\left[\Lambda\left(C^{\dagger} - \alpha T^{\dagger}\right)\frac{1}{h}\frac{\partial h}{\partial t}\right]' + K\alpha\frac{H'}{\rho c_p h} - \frac{K}{h}[(E-P)C]' - KB' - \mathbf{u}'\cdot\nabla\overline{F}, \tag{8}$$

where primes denote deviations from the seasonal cycle, $\overline{\mathbf{u}}$ is the mean flow velocity, and $\nabla\overline{F}$ is the mean seasonal gradient of the flux. We have expanded the Lagrangian derivative and linearized the advection term, assuming that anomalies are small compared to the seasonal cycle. As a result, we are left with the local rate of change, mean advection, and anomalous advection terms. Of these the first two are written on the left-hand side in (8); they represent the rate of change of the flux into a parcel of fluid following the mean flow. The anomalous advection term is moved to the right-hand side since it acts as a forcing mechanism for particles following the mean flow, through advection of the mean disequilibrium tracer concentration by anomalous Ekman currents.

[26] Monthly averaged anomaly fields from the GCM (e.g., heat fluxes, mixed layer depth, and biological production) are used to estimate the forcing terms in (8), which is then solved numerically for F'. We consider the variability of fluxes following a particle traveling around Antarctica, along the geostrophic streamline shown in Figure 2. For the mean advection velocity we take the value of the mean geostrophic flow speed in the ACC, $\overline{\mathbf{u}}$ = 8 cm/s [*Verdy et al.*, 2006]. The timescale for equilibration of dissolved gases is a function of the gas transfer coefficient, mixed layer depth, and, for carbon, seawater chemistry. For a mixed layer depth of 75 m and a gas transfer coefficient of $K = 3 \times 10^{-5}$ m/s the e-folding timescale for oxygen equilibration is about 1 month. Carbonate chemistry causes the equilibration timescale for carbon to be about an order of magnitude greater, and so here we impose a timescale of 1 year by setting $K = 2.5 \times 10^{-6}$ m/s.

[27] The fluxes estimated from (8) are compared with the fluxes calculated from the GCM. Figure 7 shows the nonseasonal air-sea gas fluxes following a particle that was located at 0° longitude in January 1993 and travels along the ACC (as depicted by the dashed line) until December 2003, at which time it is situated at 36°E. In Figures 7b and 7c, solid black lines show results from the idealized model (8), which will be referred to as the Lagrangian model; the solid gray line shows results from the GCM. The magnitude and broad patterns of the variability are captured well, given the simplicity of the model and the assumptions made. The agreement is particularly good for the oxygen fluxes, which exhibit mostly high-frequency variability, in concert with heat flux anomalies. Carbon fluxes simulated with the Lagrangian model capture the low-frequency variability of the GCM field; fluctuations on shorter timescales are filtered out by the Lagrangian model as a result of the parameterized slow equilibration time of the tracer. The fast variability found in the GCM probably results from dynamical processes not taken into account in our simple Lagrangian model: For instance, the mixed layer is assumed to be actively mixing at all times, and advection is only crudely represented.

[28] By solving (8) for other initial longitudes we recreate the time longitude diagrams of Figure 3 with reasonable agreement (not shown). Following a single particle allows us to compare the magnitude of the fluxes induced by the different mechanisms. Figure 7 shows the thermal (dashed line) and entrainment (circles) components of the flux. Clearly, entrainment is the dominant forcing for both CO_2 and O_2. Thermodynamic effects are small in comparison, and other forcing terms in (8) have a negligible impact on the fluxes simulated with the Lagrangian model. Ekman advection of tracer is, to leading order, balanced by the advection of temperature, such that $\mathbf{u}' \cdot \overline{C} \approx \mathbf{u}' \cdot \overline{C^{\mathrm{sat}}}$; thus the anomlaous advection of disequilibrium tracer concentration, the last term in (8), is small. Indirectly, gas fluxes also result from meridional Ekman currents as they exchange heat with the atmosphere, but this is included in the thermal solubility term. Evaporation and precipitation effects are highly variable in time and in space; consequently, they are mostly filtered out by the simple model. Finally, we find that the Southern Ocean region of our GCM simulation exhibits very little interannual variability in biological productivity, and the diagnosed B' is negligible. Other studies also find that the effects of biology on interannual variability in ocean pCO_2 and air-sea fluxes of CO_2 are small [*Le Quéré et al.*, 2003; *Lovenduski et al.*, 2007; *Lenton and Matear*, 2007].

4.3. Further Simplifications to the Diagnostic Framework

[29] These results suggest that the large-scale patterns of oxygen and carbon dioxide flux variability can be accounted for by entrainment of deep water into the mixed layer and depleted in oxygen; interannual variability in the strength of this mixing causes anomalous air-sea gas fluxes. In light of these findings we consider the equation for the disequilibrium tracer concentration (7) in the absence of dilution and biological production. We then have

$$\frac{D\Delta C}{Dt} = -\frac{1}{\tau}\Delta C - \alpha\frac{DT}{Dt} + \Lambda(C_{th} - C)\frac{1}{h}\frac{\partial h}{\partial t}, \qquad (9)$$

where we have defined an equilibration timescale $\tau = (h/K)$: This is the time taken for the decay of disequilibrium concentrations through air-sea fluxes. There are two limit cases.

[30] 1. In the first case, $\tau \to 0$: The tracer equilibrates rapidly, and thus $\Delta C \to 0$, and the rate of change of ΔC can be neglected. The balance is primarily between the air-sea flux and the forcing: $\Delta C \sim \{DT/Dt, \partial h/\partial t\}$. The timescale of tracer flux variability approaches that of heat flux variability since heat fluxes are responsible for changes in SST and MLD. This is what we find for oxygen.

[31] 2. In the second case, $\tau \to \infty$: The tracer equilibrates slowly, and thus air-sea fluxes can be neglected. The balance is then between $\Delta C/Dt$ and the forcing terms: $\Delta C \sim \{T, h\}$. For carbon dioxide we find an intermediate response in between these two limit cases. Although carbon dioxide has a finite equilibration timescale, it responds slowly compared to the timescale of SST and MLD variability; this explains the similitude of CO_2 fluxes with SST and, to a certain extent, MLD as discussed in section 2.

5. Conclusions

[32] We have used results from a physical-biogeochemical model to examine the variability of carbon dioxide and

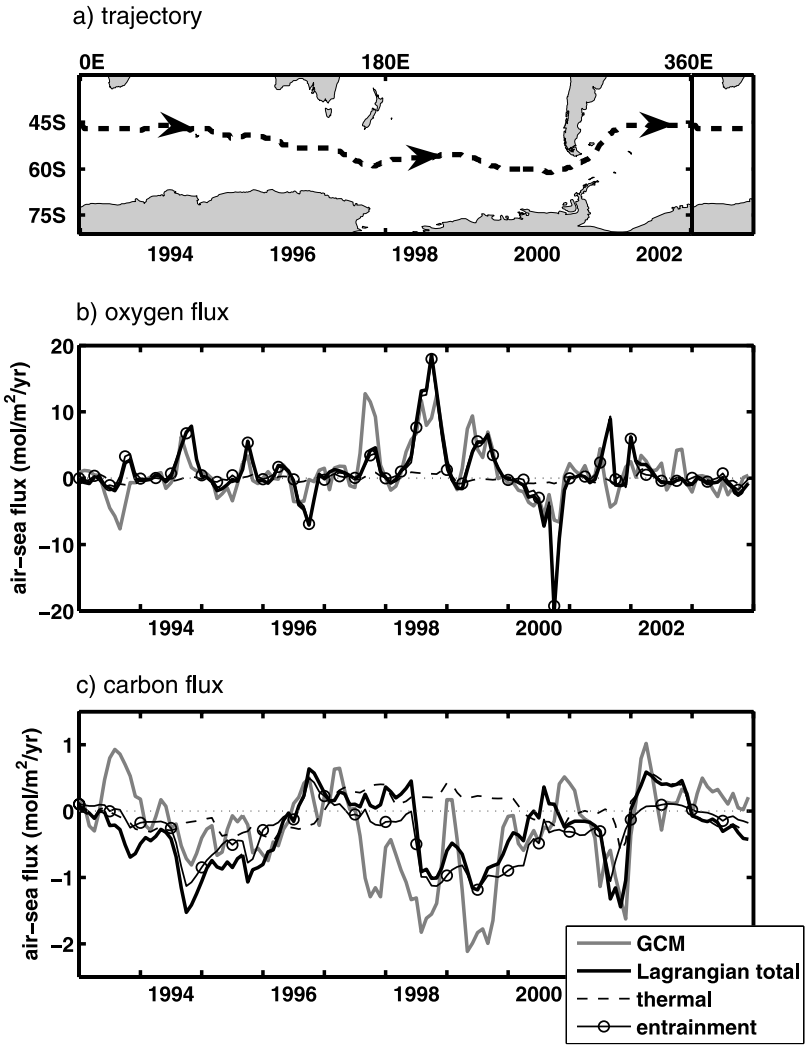

Figure 7. Variability of air-sea fluxes following a particle along a geostrophic streamline. (a) Trajectory of the particle starting at 0°E in January 1993 and propagating eastward. Years indicate time of passage at the corresponding longitude; note that longitudes 0°–36°E are repeated, with vertical line indicating 0°E. (b) O_2 fluxes and (c) CO_2 fluxes obtained using GCM (solid gray line) and obtained using equation (8) (solid black line). Contribution is due to thermal fluxes (dashed line) and entrainment fluxes (circles) from equation (8). Fluxes resulting from dilution ($E - P$), biological production, and Ekman advection are small and are not shown. Time axes are aligned in Figures 7a–7c such that spatial location of the air-sea fluxes can be inferred from Figure 7a.

oxygen air-sea fluxes in the Southern Ocean. As with earlier studies [*Lenton and Matear*, 2007; *Lovenduski et al.*, 2007] we find a strong link between carbon dioxide flux variability and the Southern Annular Mode (SAM). However, not emphasized in previous studies, we also find a strong correlation with ENSO. This suggests that both SAM and ENSO should be taken into account when addressing the ocean's response to atmospheric forcing; an analogous conclusion was reached from analyzing the Southern Ocean SST variability (see *Verdy et al.* [2006, Figure 10] for the SST response to ENSO and SAM).

[33] In the region of the ACC we find that ocean circulation strongly impacts the nonseasonal variability of CO_2 and O_2 air-sea fluxes in the GCM. This highlights the importance of capturing the physical processes accurately in models of the ocean biogeochemistry. By incorporating observations from many different sources the ECCO state estimation aims at obtaining simulated dynamical fields that are close to the true ocean state.

[34] On the other hand, the time series available are relatively short, and our analysis relies on only 11 years of simulated fields. It is possible that the spatial patterns of ENSO and SAM variability would be different for other time periods. We do, however, find our results to be consistent with the SAM and ENSO patterns of CO_2 variability in the model of *McKinley et al.* [2003], which uses the MIT general circulation model flow fields and a biogeochemical model similar to ours in a simulation that

extends to the period 1980–1998. The same Pacific-intensified patterns with a dipolar structure appear in both models.

[35] We have also used a simple Lagrangian representation of CO_2 and O_2 flux variability. It captures the main features of the variability simulated with a higher-complexity GCM; this is quite remarkable given the simplicity of the framework. Many assumptions have been made in deriving the Lagrangian model; we would not argue that it captures the true variability of tracer concentrations in the mixed layer. It does, however, serve the point of giving an estimated order of magnitude for the air-sea fluxes induced by different forcing mechanisms. The Lagrangian model allows us to examine the leading order causes of the large-scale variability and suggests that at least in this simulation, biological effects are small compared to the entrainment of deep water into the mixed layer. Thermal effects have a small but not negligible effect on the variability, especially for CO_2 with its longer equilibriation timescale. Other processes are found to have a negligible impact on the large-scale patterns of variability. Our analysis being restricted to the ACC region, we acknowledge that the mechanisms in other parts of the Southern Ocean might be quite different, in particular in coastal regions.

[36] If entrainment and thermal solubility are the main drivers as suggested in this study, one can derive an elegant expression for disequilibrium gas concentrations in the surface waters (equation (9)) involving air-sea heat fluxes and the mean geostrophic flow. These may be deduced from satellite data and, along with mixed layer depth variability estimated from a mixed layer model forced with remotely observed heat fluxes and winds, could provide a means to estimate some aspects of the variability of air-sea CO_2 and O_2 fluxes from space.

[37] **Acknowledgments.** This is a contribution of ECCO, funded by the National Oceanographic Partnership Program. We thank Galen McKinley for sharing model results and two reviewers for helpful comments on an earlier version of the manuscript. M.J.F. thanks Ric Williams for many stimulating discussions. This work was supported by the Academic Programs Office of the MIT–WHOI Joint Program in Oceanography, an NSF grant from the Office of Polar Programs to J.M. and M.J.F., and an NSF grant OCE-336839 to M.J.F. and S.D.

References

Cane, M., S. Zebiak, and S. Dolan (1986), Experimental forecasts of El-Niño, *Nature*, *321*, 827–832.

Dutkiewicz, S., A. Sokolov, J. Scott, and P. Stone (2005), A three-dimensional ocean-seaice-carbon cycle model and its coupling to a two-dimensional atmospheric model: Uses in climate change studies, *Rep. 122*, Joint Program on the Sci. and Policy of Global Change, Mass. Inst. of Technol., Cambridge.

Feely, R. A., et al. (2002), Seasonal and interannual variability of CO_2 in the equatorial Pacific, *Deep Sea Res., Part II*, *49*, 2443–2469.

Follows, M. J., S. Dutkiewicz, and T. Ito (2006), On the solution of the carbonate system in ocean biogeochemistry models, *Ocean Modell.*, *12*, 290–301.

Gent, P. R., and J. C. McWilliams (1990), Isopycnal mixing in ocean circulation models, *J. Phys. Oceanogr.*, *20*, 150–155.

Gruber, N., C. D. Keeling, and N. R. Bates (2002), Interannual variability in the North Atlantic Ocean carbon sink, *Science*, *298*, 2374–2378.

Hall, A., and M. Visbeck (2002), Synchronous variability in the Southern Hemisphere atmosphere, sea ice, and ocean resulting from the annular mode, *J. Clim.*, *15*, 3043–3057.

Key, R. M., A. Kozyr, C. L. Sabine, K. Lee, R. Wanninkhof, J. L. Bullister, R. A. Feely, F. J. Millero, C. Mordy, and T.-H. Peng (2004), A global ocean carbon climatology: Results from Global Data Analysis Project (GLODAP), *Global Biogeochem. Cycles*, *18*, GB4031, doi:10.1029/2004GB002247.

Kraus, E. B., and J. S. Turner (1967), A one dimensional model of the seasonal thermocline, Part II, *Tellus*, *19*, 98–105.

Large, W. G., J. C. McWilliams, and S. C. Doney (1994), Oceanic vertical mixing: A review and a model with a nonlocal boundary layer parameterization, *Rev. Geophys.*, *32*, 363–403.

Lenton, A., and R. Matear (2007), The role of the Southern Annular Mode (SAM) in Southern Ocean CO_2 uptake, *Global Biogeochem. Cycles*, doi:10.1029/2006GB002714, in press.

Le Quéré, C., O. Aumont, P. Monfray, and J. Orr (2003), Propagation of climatic events on ocean stratification, marine biology, and CO_2: Case studies over the 1979–1999 period, *J. Geophys. Res.*, *108*(C12), 3375, doi:10.1029/2001JC000920.

Lovenduski, N. S., and N. Gruber (2005), Impact of the Southern Annular Mode on Southern Ocean circulation and biology, *Geophys. Res. Lett.*, *32*, L11603, doi:10.1029/2005GL022727.

Lovenduski, N. S., N. Gruber, S. C. Doney, and I. D. Lima (2007), Enhanced CO_2 outgassing in the Southern Ocean from a positive phase of the Southern Annular Mode, *Global Biogeochem. Cycles*, doi:10.1029/2006GB002900, in press.

Marshall, J., A. Adcroft, C. Hill, L. Perelman, and C. Heisey (1997), A finite-volume, incompressible Navier Stokes model for studies of the ocean on parallel computers, *J. Geophys. Res.*, *102*, 5753–5766.

McKinley, G. A., M. J. Follows, J. Marshall, and S. Fan (2003), Interannual variability of air-sea O_2 fluxes and the determination of CO_2 sinks using atmospheric O_2/N_2, *Geophys. Res. Lett.*, *30*(3), 1101, doi:10.1029/2002GL016044.

McKinley, G. A., M. J. Follows, and J. Marshall (2004), Mechanisms of air-sea CO_2 flux variability in the equatorial Pacific and the North Atlantic, *Global Biogeochem. Cycles*, *18*, GB2011, doi:10.1029/2003GB002179.

Parekh, P., M. Follows, S. Dutkiewicz, and T. Ito (2006), Physical and biological regulation of the soft tissue carbon pump, *Paleoceanography*, *21*, PA3001, doi:10.1029/2005PA001258.

Redi, M. H. (1982), Oceanic isopycnal mixing by coordinate rotation, *J. Phys. Oceanogr.*, *12*, 1154–1158.

Takahashi, T., J. Olafsson, J. Goddard, D. W. Chipman, and S. C. Sutherland (1993), Seasonal variation of CO_2 and nutrients in the high-latitude surface oceans: A comparative study, *Global Biogeochem. Cycles*, *7*, 843–878.

Thompson, D., and J. Wallace (2000), Annular modes in the extra-tropical circulation. Part I: Month-to-month variability, *J. Clim.*, *13*, 1000–1016.

Verdy, A., J. Marshall, and A. Czaja (2006), Sea surface temperature variability along the path of the Antarctic circumpolar current, *J. Phys. Oceanogr.*, *36*, 1317–1331.

Wanninkhof, R. (1992), Relationship between wind speed and gas exchange over the ocean, *J. Geophys. Res.*, *97*, 7373–7382.

Williams, R. G., and M. J. Follows (1998), The Ekman transfer of nutrients and maintenance of new production over the North Atlantic, *Deep Sea Res., Part I*, *45*, 461–489.

Wunsch, C., and P. Heimbach (2006), Estimated decadal changes in the North Atlantic meridional overturning circulation and heat flux 1993–2004, *J. Phys. Oceanogr.*, *36*, 2012–2024.

Yuan, X. (2004), ENSO-related impacts on Antarctic sea ice: A synthesis of phenomenon and mechanisms, *Antarct. Sci.*, *16*, 415–425.

A. Czaja, Space and Atmospheric Group, Department of Physics, Imperial College London, London SW7 2AZ, UK. (a.czaja@imperial.ac.uk)

S. Dutkiewicz, M. J. Follows, and J. Marshall, Department of Earth, Atmospheric and Planetary Sciences, Massachusetts Institute of Technology, 77 Massachusetts Avenue, Cambridge, MA 02139, USA. (stephd@ocean.mit.edu; mick@plume.mit.edu; marshall@gulf.mit.edu)

A. Verdy, MIT–WHOI Joint Program in Oceanography, Massachusetts Institute of Technology, 77 Massachusetts Avenue, Cambridge, MA 02139, USA. (averdy@ocean.mit.edu)